Neutron decay of ^{15}C resonances by measurements of neutron time-of-flight

M. Cavallaro,[1] C. Agodi,[1] M. Assié,[2] F. Azaiez,[2] F. Cappuzzello,[1,3] D. Carbone,[1] N. de Séréville,[2] A. Foti,[3,4] L. Pandola,[1] J. A. Scarpaci,[5] O. Sgouros,[6] V. Soukeras,[6] and S. Tropea[1]

[1]*Istituto Nazionale di Fisica Nucleare, Laboratori Nazionali del Sud, I-95125 Catania, Italy*
[2]*Institut de Physique Nucléaire, Université Paris-Sud-11-CNRS/IN2P3, 91406 Orsay, France*
[3]*Dipartimento di Fisica e Astronomia, Università di Catania, I-95125 Catania, Italy*
[4]*Istituto Nazionale di Fisica Nucleare, Sezione di Catania, I-95125 Catania, Italy*
[5]*Centre de Sciences Nucléaires et de Sciences de la Matières-CSNSM, Université Paris-Sud-11-CNRS/IN2P3, 91405 Orsay, France*
[6]*Department of Physics and HINP, The University of Ioannina, 45110 Ioannina, Greece*

(Received 24 September 2015; revised manuscript received 27 April 2016; published 27 June 2016)

The neutron decay of the resonant states of light neutron-rich nuclei is an important and poorly explored property, useful to extract valuable nuclear structure information. In the present paper the neutron decay of the ^{15}C resonances populated via the two-neutron transfer reaction ^{13}C(^{18}O,^{16}O n) at 84-MeV incident energy is reported for the first time using an innovative technique which couples the MAGNEX magnetic spectrometer and the EDEN neutron detector array. Experimental data show that the resonances below the one-neutron emission threshold decay to the ^{14}C ground state via one-neutron emission with an almost 100% total branching ratio, whereas the recently observed ^{15}C giant pairing vibration at 13.7 MeV mainly decays via two-neutron emission.

DOI: 10.1103/PhysRevC.93.064323

I. INTRODUCTION

The investigation of the decay modes of nuclear states populated in direct reactions is a powerful tool for understanding their microscopic structures. When the reaction populates unbound or weakly bound neutron-rich systems, the neutron emission is the dominant decay mode of the excited states and sometimes of the ground state itself. In these cases, the coincidence detection of the emitted neutrons and charged ejectiles and the high-resolution measurement of the neutron energy are crucial tasks for spectroscopic investigations of the residual nuclei.

The recent advent of large acceptance magnetic spectrometers [1–5] has allowed a deeper exploration of stable and unstable nuclei up to high excitation energy with considerable resolution and good statistical significance, leading to the observation of new resonances in the unknown continuum. Examples are the giant pairing vibrations (GPVs) which are collective motions in the particle-particle space excited via two-neutron transfer reactions. Signatures of such resonances in light nuclei, such as ^{14}C and ^{15}C have been recently discussed in Refs. [6–8]. Other structures in the continuum generated by nucleon-nucleon correlations beyond the mean field have also been predicted and/or experimentally observed [9–14]. The availability of radioactive ion-beam facilities and the possibility to measure charged particle energy spectra with high resolution has given access to neutron unbound nuclei whose structures are still controversial [15,16].

In this context the study of the carbon isotopic chain has attracted a long-standing interest since it allows for giving quantitative information on the role of single-particle, nucleon pairing, and cluster degrees of freedom in atomic nuclei. An interesting case is ^{15}C, characterized by a small separation energy of the valence neutron ($S_n = 1.218$ MeV), intermediate between one of the well-bound $^{12-14}$C nuclei and one of the more exotic neutron-rich isotopes towards the drip lines [17–19]. The properties of the ^{15}C ground state [20–23] and excited states [24] are subjects of debate. For example, between S_n and the two-neutron separation energy ($S_{2n} = 9.394$ MeV), narrow resonances characterized by configurations of a two-neutron pair on a ^{13}C core are typically excited on the top of the continuum of the ^{14}C $+ n$ system by (t,p) and (^{18}O, ^{16}O) reactions [25,10]. Above S_{2n}, where the ^{13}C $+2n$ system is also unbound, a supplementary continuous distribution is found. Narrow resonances with three-particle-four-hole structures are observed in multinucleon transfer reactions [17,26,27] whereas pairing excitations are populated in two-neutron transfer processes. In general, multi-particle-multi-hole configurations are mixed in the continuum, resulting in a nontrivial prediction of the decay properties of the resonances. Thus, experimental measurements of the decay modes are the only way to determine the branching ratios, adding significant information to the spectroscopic features extracted in inclusive experiments.

In this paper we study for the first time the neutron decay of the ^{15}C resonances above S_n up to 16-MeV excitation energy, populated via the ^{13}C(^{18}O,^{16}O n) reaction at 84-MeV incident energy. The neutron kinetic energy is determined by time-of-flight (TOF) in an exclusive experiment by using the MAGNEX magnetic spectrometer and the EDEN neutron detector array. Section II describes the setup, the experiment, and the data analysis. In Sections III and IV the measured neutron decay spectra and branching ratios are shown and discussed.

II. THE EXPERIMENT

A. The experimental apparatus

A standard method to determine the neutron kinetic energy is to measure the TOF along a known path length. This technique is optimized in facilities as nTOF at CERN where a very long flight path (200 m) is available [28]. The TOF *start* timing signal is usually generated exploiting the periodic

structure of a pulsed beam. This determines the presence of convoluted components in the final TOF spectrum, making the data reduction and the extraction of physical information more involved. An alternative approach is the use of devoted *start* detectors close to the target. However rate limitations arise from the use of such detectors at very forward angles (including 0°) under beams more intense than 10^5–10^6 pps. In addition, the degrading effect produced by the detector active materials and dead layers upstream of an analyzing magnet can deteriorate the overall energy and angular resolution, especially for low-energy heavy ions. Finally the limited efficiency of the detector could be an issue when dealing with low count-rate experiments.

In the TOF technique used in the present paper, the *start* signal is given by the detection of the ejectiles at the focal plane of the MAGNEX magnetic spectrometer. The *stop* signal is provided by the EDEN neutron detector's time signal, delayed by a known quantity. The novelty of the present technique is that the ion path length along the spectrometer is extracted event by event by solving the equation of motion of the ions detected at the focal plane and reconstructing the complete ion trajectory.

The MAGNEX spectrometer consists of two magnetic elements: a large aperture quadrupole (20-cm radius), providing focusing strength on the vertical plane, and a large bending magnet (20-cm gap), ensuring momentum dispersion and horizontal focus. It is characterized by large acceptance both in angle (solid angle $\Delta\Omega = 50$ msr) and in momentum (relative momentum with respect to the central trajectory $\Delta p = -14\%, +10\%$). The features and performances of MAGNEX are described in Refs. [29–34]. The high-order aberrations originated by the large acceptance are calculated and corrected by means of a software ray reconstruction based on COSY INFINITY [35] described in Refs. [36–41]. The reaction ejectiles, momentum analyzed by MAGNEX, are detected by the focal plane detector (FPD). It consists of a gas drift chamber divided in five sections, each one working also as a proportional counter and four of which being position-sensitive. A wall of 60 stopping silicon pad detectors is located at the back of the gas section. The logic OR of the signals from the silicon detectors is used to measure the TOF of the particles moving through the spectrometer. It also gives the trigger of the whole acquisition system. A detailed description of the MAGNEX FPD is reported in Ref. [42].

EDEN is an array of 36 cylindrical organic scintillators (NE213), 5-cm thick with 20-cm diameter, located around the MAGNEX scattering chamber. In the experiment they were positioned at a distance ranging from 1.8 to 2.4 m from the target, covering a total solid angle of 270 msr corresponding to laboratory angles from −58° to −71°, from +103° to +146° on the reaction plane, and from −13° to +29° out of the reaction plane. A detailed description of the detectors and photomultipliers layout is given in Ref. [43]. The neutron-γ discrimination is provided by pulse-shape analysis of the fast and slow components of the scintillation signal. It allows a low detection threshold (30 keV*ee*) and a good neutron-γ separation at low deposited energies, thus maximizing the neutron detection efficiency. A specific readout electronics, based on fast stretcher modules named BaFPro, was developed for this purpose as discussed in detail in Ref. [44]. A timing signal generated by a constant fraction discriminator is also an output of the module for each EDEN channel. In order to measure the neutron TOF and hence the energy, the EDEN timing signal is sent to a high-stability delay line which introduces a delay of $\Delta T_{\rm delay} = 400$ ns and then to the *stop* input of a time to digital converter (TDC). The common *start* to the TDC is given by the logic OR of the timing signals of the MAGNEX silicon detectors. Thus, once the time-of-flight of the charged ejectiles along the spectrometer is known ($\mathrm{TOF_{ion}}$), the time-of-flight of the neutrons from the target point to the EDEN detector ($\mathrm{TOF_{EDEN}}$) can be deduced.

B. Experiment and data reduction

The experiment was performed at INFN-Laboratori Nazionali del Sud using a $^{18}O^{6+}$ beam delivered by the Tandem Van der Graff accelerator at 84-MeV incident energy impinging on a 50-μg/cm^2 99% enriched ^{13}C target. The ^{17}O and ^{16}O reaction ejectiles were momentum analyzed by MAGNEX in two separate runs. Data on the ^{12}C target were also collected to take the ^{12}C contaminant in the used target into account. The explored angular range was $3° < \theta_{\rm lab} < 14°$ in the laboratory reference frame. The ejectiles were identified at the FPD as described in Ref. [45] and their momentum reconstructed by the ray-reconstruction technique [37]. The excitation energy spectra of the reaction products were obtained by the missing mass method $E_x = Q_0 - Q$ (where Q_0 is the ground to ground-state reaction Q value).

For each event reaching the FPD, the path length of the ion along the spectrometer l_f and its momentum are reconstructed by the ray reconstruction and consequently its time-of-flight $\mathrm{TOF_{ion}}$ extracted. The time difference ($T_{\rm TDC}$) between the MAGNEX (common *start*) and the EDEN (*stop*) time signals, delayed by a fixed quantity $\Delta T_{\rm delay} = 400$ ns, was also available, event by event, by the readout of 36 TDC channels. The effective time-of-flight $\mathrm{TOF_{EDEN}}$ of the neutrons (or γ rays) from the target point where the nuclear reaction takes place to each EDEN detector was deduced by the relation,

$$\mathrm{TOF_{EDEN}} = \mathrm{TOF_{ion}} + T_{\rm TDC} - \Delta T_{\rm delay}, \qquad (1)$$

as schematically represented in Fig. 1.

The ^{13}C(^{18}O, ^{17}Oγ)^{14}C data were used to test the time-of-flight resolution. The ^{17}O ejectiles were identified by the MAGNEX FPD [45], and the γ rays were detected by EDEN and selected in the fast-slow representation as shown in Fig. 2(a) [44]. A narrow peak corresponding to the presence of γ rays produced in the target appears in the EDEN time spectra ($\mathrm{TOF_{EDEN}}$) as displayed in Fig. 2(b). The peak is fitted by a Gaussian function, and a full width at half maximum of 2.4 ns is extracted, which is the achieved time resolution. This value is compatible with the intrinsic resolution of an EDEN scintillator coupled to a MAGNEX silicon detector, thus making the aberration's compensation performed by the trajectory reconstruction quite satisfactory. The γ peak in Fig. 2(b) is centered at 6.1 ns, which corresponds to the γ-ray time-of-flight in 1.8-m distance between the target point and the considered EDEN detector.

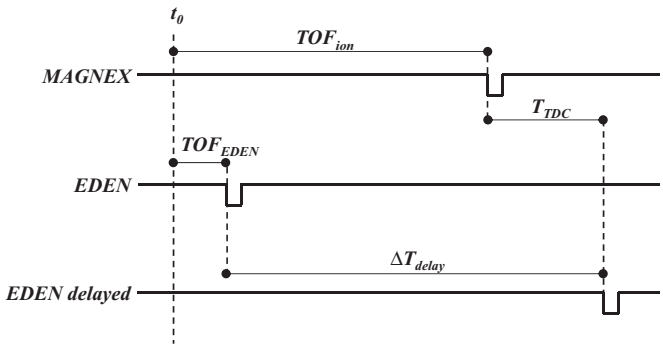

FIG. 1. Schematic of the time diagram used for the determination of the time-of-flight of the neutrons (or γ rays) $\mathrm{TOF_{EDEN}}$ from the target point to each EDEN detector [see Eq. (1)]. t_0 is the time at which the reaction takes place. T_{TDC} is the time difference between the FPD and the EDEN time signal delayed by a fixed quantity $\Delta T_{\mathrm{delay}}$.

The timing electronic chain of the 36 EDEN detectors was calibrated sending pulses at known times in a range of 1.28 μs. An offset adjustment was then applied for each EDEN detector and for each silicon detector by using the γ-peak position to take into account the differences in the electronic chains.

Once the neutrons are identified against the γ rays and their times-of-flight are extracted, the knowledge of the distances and angles of the EDEN array with respect to the target allows for determining the kinetic energy of the neutrons by relativistic relations. For the study of the decay mode of resonances populated in transfer reactions, one needs to measure the neutrons decaying from the residual nuclei. The neutron velocity $\vec{v}_n$ and energy E_n must be determined in the reference frame of the decaying nucleus, according to

$$\vec{v}_n = \vec{v}_n^{\mathrm{LAB}} - \vec{v}_{\mathrm{nucleus}}^{\mathrm{LAB}}, \tag{2}$$

$$E_n = m_n c^2 \left(\frac{1}{\sqrt{1 - \left(\frac{v_n}{c}\right)^2}} - 1 \right), \tag{3}$$

where m_n is the neutron mass, $\vec{v}_{\mathrm{nucleus}}^{\mathrm{LAB}}$ is the velocity of the residual nucleus in the laboratory reference frame obtained by the ray reconstruction in MAGNEX, and $\vec{v}_n^{\mathrm{LAB}}$ is the neutron velocity in the laboratory. Its modulus is $v_n^{\mathrm{LAB}} = \frac{d}{\mathrm{TOF_{EDEN}}}$, where d is the distance between the target and the half thickness of each EDEN detector. The real point inside the scintillator where the collision with the proton takes place is known within 5 cm (which is the scintillator thickness) for neutrons emitted orthogonally to the front face of the detector. This introduces about 6% uncertainty in the neutron kinetic-energy determination. Taking into account also the uncertainty of the distance measurement procedure ($\pm$1 cm) and the estimated time resolution, the neutron kinetic-energy resolution reaches about 10%. The inaccuracies in the reconstruction of the ion path determine a supplementary contribution of 15%.

The ^{13}C(^{18}O,^{16}O n) reaction was explored to study the neutron decay modes of the ^{15}C resonances. Figure 3 shows the $\mathrm{TOF_{EDEN}}$ spectrum for all the EDEN and silicon detectors with conditions on the identification of the ^{16}O ejectiles in MAGNEX. The γ-ray peak at about 5 ns $< \mathrm{TOF_{EDEN}} <$ 9 ns and a bump due to the presence of correlated neutrons are visible at $\mathrm{TOF_{EDEN}} \sim$ 90 ns above a flat uncorrelated background.

An estimation of the background due to the presence of uncorrelated neutrons and γ rays was obtained by generating randomly distributed TDC events ($T_{\mathrm{TDC}}^{\mathrm{random}}$). Equation (1) was then applied to simulate the randomly distributed times-of-flight measured by the EDEN detectors $\mathrm{TOF_{EDEN}^{random}}$. The $\mathrm{TOF_{EDEN}^{random}}$ spectrum was normalized to $\mathrm{TOF_{EDEN}}$ in the region $\mathrm{TOF_{EDEN}} >$ 500 ns and $\mathrm{TOF_{EDEN}} <$ $-$40 ns as shown in Fig. 3. The corresponding random distribution of the neutron energy (E_n^{random}) is also obtained applying Eqs. (2) and (3).

III. STUDY OF THE ^{15}C RESONANCES

An example of the reconstructed excitation energy spectrum (E_x) of the ^{15}C system populated via the (^{18}O, ^{16}O) reaction is shown in Fig. 4. Several narrow peaks corresponding to known low-lying bound and resonant states of ^{15}C are observed. A schematic level diagram of the carbon isotopes of interest in the description of the ^{15}C neutron decay is displayed in Fig. 5. Above the one-neutron separation energy of ^{15}C, S_n, the

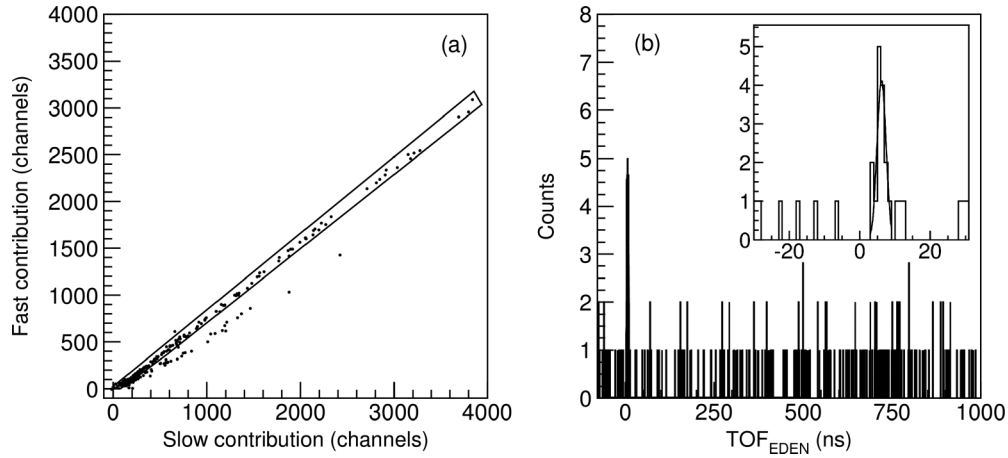

FIG. 2. (a) Example of *fast* versus *slow* distribution relative to a single EDEN detector and a single silicon detector for the ^{13}C(^{18}O,^{17}O) data. (b) Plot of $\mathrm{TOF_{EDEN}}$ for the events gated on γ rays as drawn in panel (a). In the inset a zoomed view of the $\mathrm{TOF_{EDEN}}$ plot is shown.

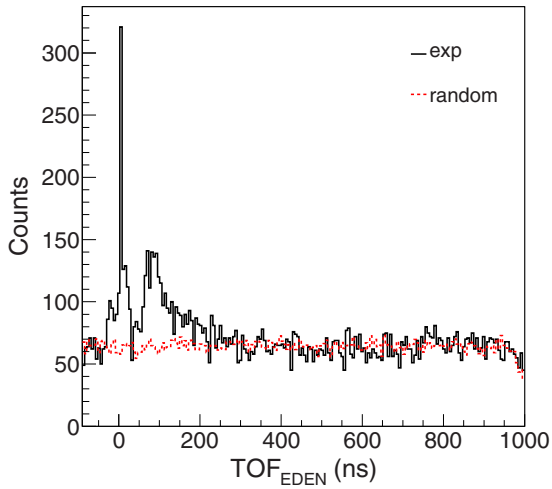

FIG. 3. Neutron time-of-flight TOF$_{EDEN}$ gated on the ^{16}O ejectiles detected by MAGNEX (black spectrum) superimposed on the randomly distributed background TOF$^{random}_{EDEN}$ (red dashed spectrum).

neutron decay of the observed resonances was studied gating on the different peaks of the ^{15}C excitation energy spectrum (E_x) and plotting the correspondent neutron energies (E_n) as shown in Figs. 6 and 7. The background neutron energy spectra (E_n^{random}) are obtained applying to the randomly distributed TOF$^{random}_{EDEN}$ the same kinematic transformations from time to energy used for the measured data (TOF$_{EDEN}$). The E_n^{random} spectra are then gated by the same conditions as E_n and subtracted in Figs. 6(b), 6(d), 6(f), 6(h), 6(j) and 7(b) and 7(d). The same scaling factor extracted from the normalization of TOF$^{random}_{EDEN}$ (Fig. 3) is used in the subtractions. The gates on the ^{15}C peaks ensure that the observed neutrons mainly correspond to the decay of the residual nucleus.

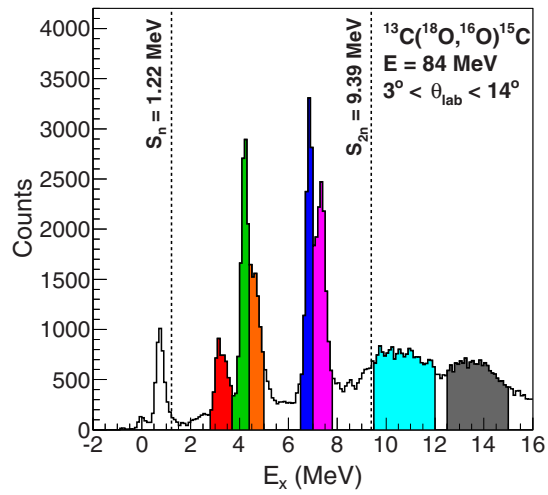

FIG. 4. ^{15}C excitation energy spectrum for the ^{13}C(^{18}O,^{16}O) reaction at 84-MeV incident energy and $3^\circ < \theta_{lab} < 14^\circ$. The color filled areas are the different regions selected for the study of the neutron decay spectra in Figs. 6 and 7. S_n and S_{2n} indicate the one- and two-neutron separation energies, respectively, of ^{15}C.

Let us consider the ^{15}C excited state at $E_x = 3.103$ MeV. The neutron energies obtained by gating the excitation energy spectrum in the region 2.9 MeV $< E_x <$ 3.6 MeV is shown in Fig. 6(a). A structure in the neutron spectrum at around 2 MeV appears in Fig. 6(b) after the subtraction of E_n^{random}, despite the large statistical error. Such an energy corresponds, within the uncertainty, to the energy of the neutrons decaying from the ^{15}C excited state at $E_x = 3.103$ MeV to the ^{14}C ground state, which is $E_n = E_x - S_n = 1.9$ MeV (see the level scheme in Fig. 5). Similarly, gating the E_x spectrum in the region of the ^{15}C state at $E_x = 4.220$ MeV (3.8 MeV $< E_x <$ 4.4 MeV), the neutron energy shows a peak centered at $E_n = E_x - S_n =$ 3 MeV [see Figs. 6(c) and 6(d)]. Gating on $E_x = 4.657$ MeV (4.4 MeV $< E_x <$ 4.9 MeV), E_n is distributed around $E_n = E_x - S_n = 3.4$ MeV [see Figs. 6(e) and 6(f)]. Also gating on the $E_x = 6.841$ MeV ^{15}C peak (6.5 MeV $< E_x <$ 7.1 MeV), a structure centered at about $E_n = E_x - S_n = 5.6$ MeV is visible in the neutron spectrum [Figs. 6(g) and 6(h)]. In this case a small fraction of the neutron distribution seems present also at lower energies, even if the statistical significance can be questionable. These results demonstrate that the investigated states in the continuum of ^{15}C mainly decay to the ^{14}C ground state. Moreover, the resulting E_n spectra give a confirmation of the reliability and accuracy of our technique to measure the neutron energy.

In the neutron spectrum gated on the ^{15}C state at $E_x =$ 7.352 MeV (7.1 MeV $< E_x <$ 7.7 MeV) shown in Figs. 6(i) and 6(j), two structures are observed. One is a peak at $E_n = E_x - S_n = 6.1$ MeV, which is likely the direct decay of ^{15}C to the ^{14}C ground state. A distribution at $E_n < 4$ MeV is also present. These low-energy neutrons can come from the neutron decay of the state of ^{14}C at 10.7 MeV, populated because of the presence of ^{12}C impurities in the used target. In this case the expected energy of such neutrons is centered at $E_n(^{14}\text{C}) = E_x(^{14}\text{C}) - S_n(^{14}\text{C}) \approx 10.7 - 8.2 = 2.5$ MeV. As studied in Ref. [10] in the same experimental conditions, such ^{14}C contaminations account for about 30% in the considered region of the inclusive spectrum. A contribution to this low-energy region could also be attributed to the decay by γ-ray emission of the ^{15}C 7.352-MeV state to the states of ^{15}C between 4 and 5 MeV with subsequent emission of neutrons of lower energy. Low-energy neutrons produced by multiple scattering in the walls of the scattering chamber can also contribute to this region.

For gating on the resonances of the E_x spectrum above the two-neutron separation energy S_{2n} (Fig. 7), a more involved interpretation is needed. First of all it is worth noting that the coincidence neutrons are centered at lower energies compared with the neutrons relative to the decay of ^{15}C resonances just below S_{2n}. In particular, the structure in the ^{15}C spectrum at 10.5 MeV was described in Ref. [10] as a resonance of the $^{13}\text{C}+n+n$ system mainly characterized by configurations with the two neutrons in the $d_{5/2}$ and $d_{3/2}$ orbitals. In case it decays by single neutron emission to the ^{14}C ground state, the neutron energies should be distributed around $E_n = E_x - S_n = 10.5 - 1.22 = 9.3$ MeV. Such neutrons are not visible in the E_n spectrum of Figs. 7(a) and 7(b). However, if ^{15}C decays to the ^{14}C states below the ^{14}C one-neutron emission threshold, namely, the group between $E'_x(^{14}\text{C}) =$

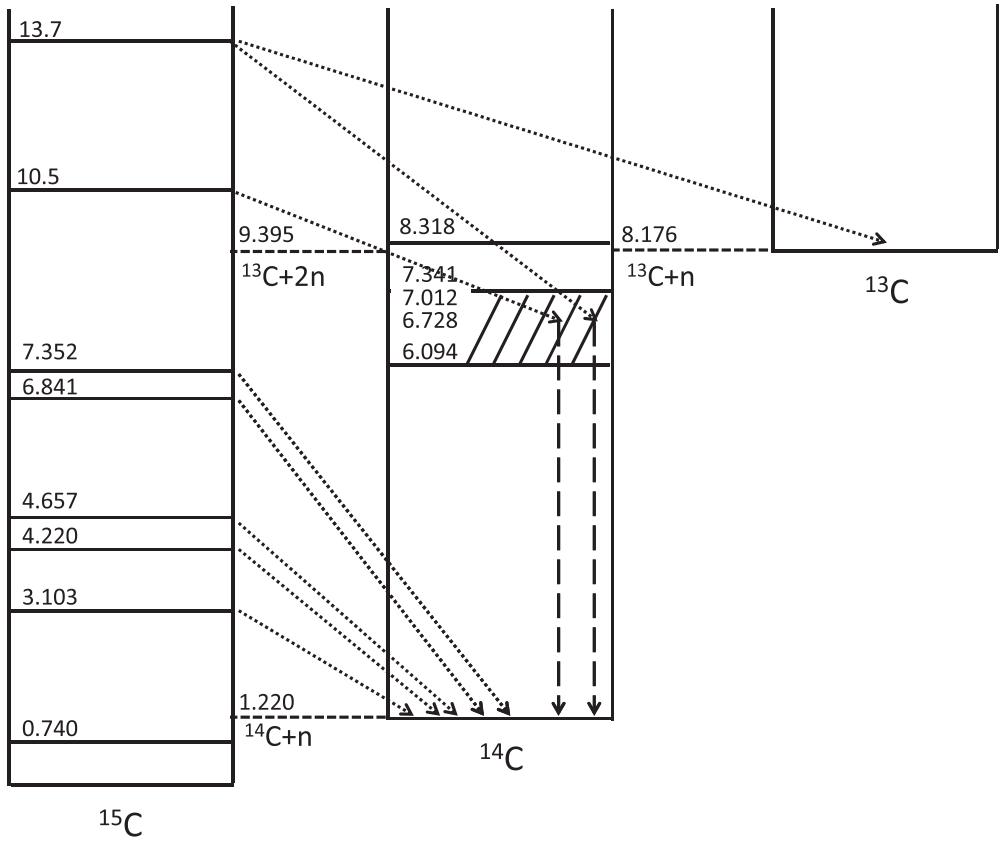

FIG. 5. ^{15}C level diagram and proposed neutron decay scheme. The observed neutron decays are indicated by dotted arrows, and the deduced γ decays are indicated by the dashed arrows.

6.094 MeV and $E_x''(^{14}\mathrm{C}) = 7.341$ MeV, the expected neutron energy would range between $E_n = E_x - E_x'(^{14}\mathrm{C}) - S_n = 3.2$ MeV and $E_n = E_x - E_x''(^{14}\mathrm{C}) - S_n = 2$ MeV, which is actually experimentally observed in Figs. 7(a) and 7(b). Regarding the direct two-neutron decay to the ^{13}C ground state, which would generate a distribution ranging from zero to $E_n = E_x - S_{2n} = 1.1$ MeV, the large error in the background subtraction at such small energies prevents drawing definite conclusions. The neutron energy spectrum shows also a small structure at ~6 MeV, statistically uncertain, which cannot be explained by neutron decay of ^{15}C only. It can be attributed to the neutron decay of the ^{14}C multiplet of states at ~14 MeV due to ^{12}C impurities in the target. The contribution of ^{14}C neutron decay is expected at neutron energies around $E_n(^{14}\mathrm{C}) = E_x(^{14}\mathrm{C}) - S_n(^{14}\mathrm{C}) \approx 14 - 8.2 = 5.8$ MeV.

The resonance in the ^{15}C spectrum at $E_x = 13.7$ MeV was associated with the giant pairing vibration in Ref. [6]. Its decay to the ^{14}C ground state and the consequent emission of neutrons of energy distributed around $E_n = E_x - S_n = 13.7 - 1.22 = 12.5$ MeV is ruled out by the measured neutron spectrum of Figs. 7(c) and 7(d). The high-energy part of the neutron spectrum can be described as the decay to the group of ^{14}C excited states between $E_x'(^{14}\mathrm{C}) = 6.094$ MeV and $E_x''(^{14}\mathrm{C}) = 7.341$ MeV, which would produce neutrons with energies distributed between 5 and 6.4 MeV. However, the most intense neutron distribution in coincidence with the GPV peak of ^{15}C is at lower energy and can be explained by the decay to the ^{13}C ground state via a two-neutron emission. In this case, neutron energies ranging from zero to $E_n = E_x - S_{2n} = 4.3$ MeV are expected and, in fact, observed. The simultaneous measurement of two-neutron coincidences is prevented by the low yields in the present experiment. However a dedicated experiment is foreseen as the next step of our research program.

IV. BRANCHING RATIOS

An analysis of the neutron decay ratios was also performed within the statistical error due to the low yields in the neutron spectra. The ratio of the total detected neutrons over the number of events populating the ^{15}C spectrum was determined. The neutron yields were corrected taking into account the EDEN detection efficiency studied in Ref. [43], ranging from 50% to 30% as a function of the energy, the solid angle covered (2.1%), and the scattering and absorption of the neutrons in the scattering chamber. In particular the effects of the 3-cm-thick steel scattering chamber were evaluated by a simplified Monte Carlo simulation based on the GEANT4 toolkit [46,47]. The simulation was configured as an isotropic beam of neutrons with initial energy ranging from 1 to 6 MeV impinging on the walls of the scattering chamber. The NeutronHP module of GEANT4 was used for the precise neutron tracking. A global integral transmission factor between 99.8% and 97.9% depending on the initial energy was obtained, in agreement

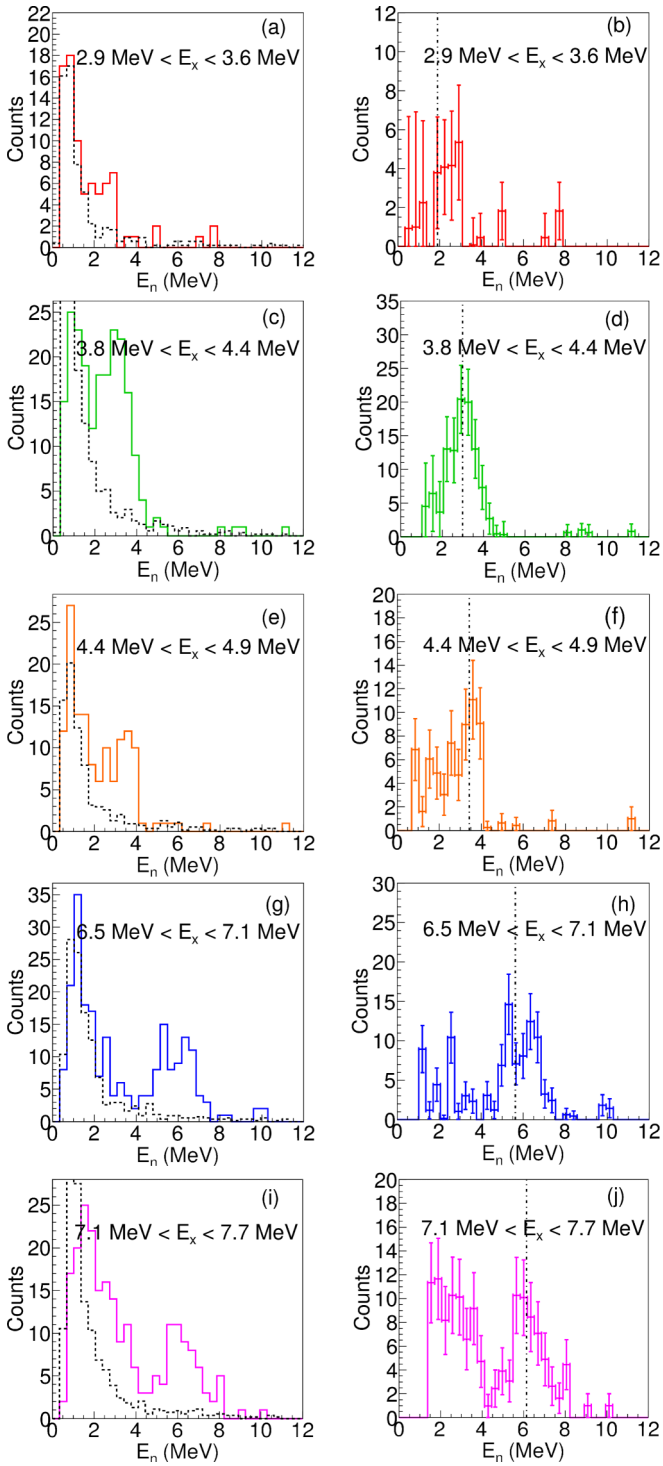

FIG. 6. (a), (c), (e), (g), and (i) Neutron energy spectra gated on different ^{15}C excitation energy regions for the experimental data (solid line) and for the randomly distributed events (dashed line). (b), (d), (f), (h), and (j) Energy spectra with background subtraction. The dot-dashed lines correspond to the decay energy of each ^{15}C state $E_n = E_x - S_n$.

with the values present in literature [48]. Multiple scattering phenomena were also taken into account in the simulation, and an average number of interactions before escaping the scattering chamber of 1.5 was estimated for each neutron.

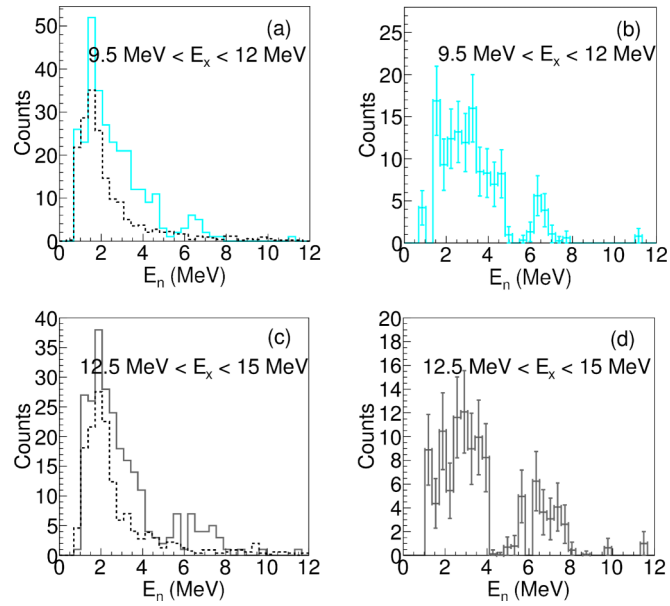

FIG. 7. (a) and (c) Neutron energy spectra gated on different ^{15}C excitation energy regions for the experimental data (solid line) and for the randomly distributed events (dashed line). (b) and (d) Energy spectra with background subtraction.

Among the transmitted neutrons, a percentage ranging from 75.8% (at 2 MeV) to 67.4% (at 6 MeV) is transmitted with the same energy within the experimental energy resolution. The remaining neutrons generate a tail in the energy spectra which increases the background at low energy.

The resulting neutron emission probability for the whole ^{15}C spectrum above S_n is $101\% \pm 8\%$, which is compatible to the values measured in Refs. [49,50]. Thanks to the high-energy resolution in the ^{15}C spectrum we can also determine the neutron emission probability for each excited state. No information is present in literature regarding the decay of the single ^{15}C excited states [51]. The ratios R of the number of detected neutrons, corrected as described above, over the number of counts for each of the ^{15}C resonances, have been measured and are listed in Table I. The error bars include

TABLE I. Neutron decay ratio for each ^{15}C state populated in the ^{13}C(^{18}O,^{16}O n) reaction. For the state at 13.7 MeV, the decay ratio for each peak and for the sum of them are detailed. The values of excitation energies E_x of the ^{15}C states are from Refs. [51,6].

^{15}C state E_x (MeV)	R
3.103	0.73 ± 0.32
4.220	0.88 ± 0.16
4.657	0.99 ± 0.21
6.841	1.15 ± 0.21
7.352	1.16 ± 0.25
10.5	0.99 ± 0.16
13.7	0.63 ± 0.13 ($E_n \leqslant 4$ MeV)
	0.34 ± 0.09 ($E_n > 4$ MeV)
	0.97 ± 0.1 (total)
Total	1.01 ± 0.08

the uncertainty on the efficiency correction estimation, on the solid angle determination, on the absorption and rescattering calculations, and a statistical contribution due the subtraction of the normalized background neutron spectrum. This latter is the dominant contribution to the overall error.

Above the two-neutron emission threshold S_{2n} the 13.7-MeV resonance decays by emitting more than a single neutron. The dominant channel is the two-neutron decay to the ^{13}C ground state, which accounts for 63% of the yield, indicating large components with two correlated neutrons on a ^{13}C core for these states in agreement with what was found in Refs. [6,52]. More data will be necessary to evaluate the geometrical distribution of the neutron-neutron decay pattern and study the spatial correlation of the pair.

V. CONCLUSIONS

The neutron decay of the ^{15}C resonances populated via the two-neutron transfer reaction ^{13}C(^{18}O ,^{16}O n) at 84 MeV is studied, and the branching ratios are reported for the first time. In the experiment, the ^{16}O ejectiles were detected by the MAGNEX spectrometer and the neutrons by the EDEN detector array in coincidence. The neutron kinetic energy was deduced by measuring the time between the MAGNEX silicon detectors and the EDEN scintillator's signals without the need for any devoted *start* detector. This is possible by reconstructing, for each event, the ions' time-of-flight through the spectrometer.

The neutron energy spectra measured in coincidence with the ^{15}C resonances below the two-neutron emission threshold show that such states mainly decay to the ^{14}C ground state. Above the two-neutron emission threshold, the neutron energy spectra in coincidence with the ^{15}C giant pairing vibration at 13.7 MeV indicate that the decay of this resonance by one-neutron emission to the ^{14}C ground state is suppressed. The GPV mainly decays (63%) to the ^{13}C ground state emitting two neutrons sharing the available energy.

The technique presented in this paper is promising for a deeper investigation of states above the neutron emission threshold. Despite the low statistics, the data show sensitivity to single-particle or more complex configurations in the studied states. In particular the role of the neutron-neutron pairing field on the decay pattern looks important. Future experiments with larger datasets are foreseen in view of the study of neutron-neutron spatial correlation in the spectra with a two-neutron multiplicity gate.

ACKNOWLEDGMENTS

O. Sgouros and V. Soukeras warmly acknowledge financial support from the LLP/ERASMUS Programme - UNIVERSITY OF IOANNINA, 2012–2013.

[1] A. Cunsolo *et al.*, Nucl. Instrum. Methods Phys. Res., Sect. A **484**, 56 (2002).
[2] A. M. Stefanini *et al.*, Nucl. Phys. A **701**, 217 (2002).
[3] D. Bazin *et al.*, Instrum. Methods Phys. Res., Sect. B **204**, 629 (2003).
[4] M. Rejmund *et al.*, Nucl. Instrum. Methods Phys. Res., Sect. A **646**, 184 (2011).
[5] T. Kobayashi *et al.*, Instrum. Methods Phys. Res., Sect. B **317**, 294 (2013).
[6] F. Cappuzzello *et al.*, Nat. Commun. **6**, 6743 (2015).
[7] J. Piekarewicz, Nat. Phys. **11**, 303 (2015).
[8] D. Carbone, Eur. Phys. J. Plus **130**, 143 (2015).
[9] D. Carbone *et al.*, Phys. Rev. C **90**, 064621 (2014).
[10] F. Cappuzzello *et al.*, Phys. Lett. B **711**, 347 (2012).
[11] S. E. A. Orrigo *et al.*, Phys. Lett. B **633**, 469 (2006).
[12] C. Nociforo *et al.*, Eur. Phys. J. A **27**, 283 (2006).
[13] R. Bijker and F. Iachello, Phys. Rev. Lett. **112**, 152501 (2014).
[14] M. Freer, Rep. Prog. Phys. **70**, 2149 (2007).
[15] I. Tanihata *et al.*, Progr. Part. Nucl. Phys. **68**, 215 (2013).
[16] Yu. Aksyutina *et al.*, Phys. Rev. Lett. **111**, 242501 (2013).
[17] H. G. Bohlen *et al.*, Eur. Phys. J. A **31**, 279 (2007).
[18] N. Kobayashi *et al.*, Phys. Rev. C **86**, 054604 (2012).
[19] K. Tanaka *et al.*, Phys. Rev. Lett. **104**, 062701 (2010).
[20] D. Bazin *et al.*, Phys. Rev. C **57**, 2156 (1998).
[21] Y. L. Parfenova, M. V. Zhukov, and J. Vaagen, Phys. Rev. C **62**, 044602 (2000).
[22] E. Sauvan *et al.*, Phys. Lett. B **491**, 1 (2000).
[23] D. Q. Fang *et al.*, Phys. Rev. C **69**, 034613 (2004).
[24] F. Cappuzzello *et al.*, Europhys. Lett. **65**, 766 (2004).
[25] S. Truong and H. T. Fortune, Phys. Rev. C **28**, 977 (1983).
[26] H. G. Bohlen *et al.*, Phys. Rev. C **68**, 054606 (2003).
[27] J. D. Garret *et al.*, Phys. Rev. C **10**, 1730 (1978).
[28] C. Guerrero *et al.*, Eur. Phys. J. A, **49**, 27 (2013).
[29] F. Cappuzzello *et al.*, Eur. Phys. J. A **52**, 167 (2016).
[30] A. Cunsolo *et al.*, Nucl. Instrum. Methods Phys. Res., Sect. A **481**, 48 (2002).
[31] F. Cappuzzello *et al.*, *MAGNEX: An Innovative Large Acceptance Spectrometer for Nuclear Reaction Studies in: Magnets: Types, Uses and Safety* (Nova, New York, 2011), pp. 1–63.
[32] A. Cunsolo *et al.*, Eur. Phys. J.: Spec. Top. **150**, 343 (2007).
[33] M. Cavallaro *et al.*, Nucl. Instrum. Methods Phys. Res., Sect. A **648**, 46 (2011).
[34] M. Cavallaro *et al.*, Nucl. Instrum. Methods Phys. Res., Sect. A **637**, 77 (2011).
[35] K. Makino, M. Berz, Nucl. Instrum. Methods Phys. Res., Sect. A **558**, 346 (2006).
[36] M. Berz, Part. Accel. **24**, 109 (1989).
[37] F. Cappuzzello *et al.*, Nucl. Instrum. Methods Phys. Res., Sect. A **638**, 74 (2011).
[38] A. Lazzaro *et al.*, Nucl. Instrum. Methods Phys. Res., Sect. A **570**, 192 (2007).
[39] A. Lazzaro *et al.*, Nucl. Instrum. Methods Phys. Res., Sect. A **585**, 136 (2008).
[40] A. Lazzaro *et al.*, Nucl. Instrum. Methods Phys. Res., Sect. A **591**, 394 (2008).
[41] A. Lazzaro *et al.*, Nucl. Instrum. Methods Phys. Res., Sect. A **602**, 494 (2009).
[42] M. Cavallaro *et al.*, Eur. Phys. J. A **48**, 59 (2012).

[43] H. Laurent *et al.*, Instrum. Methods Phys. Res., Sect. A **326**, 517 (1993).
[44] M. Cavallaro *et al.*, Instrum. Methods Phys. Res., Sect. A **700**, 65 (2013).
[45] F. Cappuzzello *et al.*, Instrum. Methods Phys. Res., Sect. A **621**, 419 (2010).
[46] S. Agostinelli *et al.*, Instrum. Methods Phys. Res., Sect. A **506**, 250 (2003).
[47] J. Allison *et al.*, IEEE Trans. Nucl. Sci. **53**, 270 (2006).
[48] K. Shure, J. A. O'Brien, and D. M. Rothberg, Nucl. Sci. Eng. **35**, 371 (1969).
[49] P. L. Reeder, R. A. Warner, W. K. Hensley, D. J. Vieira, and J. M. Wouters, Phys. Rev. C **44**, 1435 (1991).
[50] J. P. Dufour *et al.*, Z. Phys. A: At. Nucl. **319**, 237 (1984).
[51] F. Ajzenberg-Selove, Nucl. Phys. A **523**, 1 (1991).
[52] M. Cavallaro *et al.*, Phys. Rev. C **88**, 054601 (2013).